Energy landscape of self-assembled superlattices of PbSe nanocrystals

Zewei Quan[a,b], Di Wu[c], Jinlong Zhu[d], Wiel H. Evers[e,f], James M. Boncella[b], Laurens D. A. Siebbeles[e], Zhongwu Wang[g], Alexandra Navrotsky[c,1], and Hongwu Xu[a,1]

[a]Earth and Environmental Sciences Division and [b]Materials Physics and Applications Division, Los Alamos National Laboratory, Los Alamos, NM 87545; [c]Peter A. Rock Thermochemistry Laboratory and Nanomaterials in the Environment, Agriculture, and Technology Organized Research Unit, University of California, Davis, CA 95616; [d]Los Alamos Neutron Science Center, Los Alamos National Laboratory, Los Alamos, NM 87545; [e]Optoelectronic Materials Section, Department of Chemical Engineering, Delft University of Technology, 2628 BL, Delft, The Netherlands; [f]Kavli Institute for Nanoscience, Delft University of Technology, 2628 CJ, Delft, The Netherlands; and [g]Cornell High Energy Synchrotron Source, Wilson Laboratory, Cornell University, Ithaca, NY 14853

Contributed by Alexandra Navrotsky, May 13, 2014 (sent for review March 5, 2014)

Self-assembly of nanocrystals (NCs) into superlattices is an intriguing multiscale phenomenon that may lead to materials with novel collective properties, in addition to the unique properties of individual NCs compared with their bulk counterparts. By using different dispersion solvents, we synthesized three types of PbSe NC superlattices—body-centered cubic (*bcc*), body-centered tetragonal (*bct*), and face-centered cubic (*fcc*)—as confirmed by synchrotron small-angle X-ray scattering. Solution calorimetric measurements in hexane show that the enthalpy of formation of the superlattice from dispersed NCs is on the order of −2 kJ/mol. The calorimetric measurements reveal that the *bcc* superlattice is the energetically most stable polymorph, with the *bct* being 0.32 and the *fcc* 0.55 kJ/mol higher in enthalpy. This stability sequence is consistent with the decreased packing efficiency of PbSe NCs from *bcc* (17.2%) to *bct* (16.0%) and to *fcc* (15.2%). The small enthalpy differences among the three polymorphs confirm a closely spaced energy landscape and explain the ease of formation of different NC superlattices at slightly different synthesis conditions.

PbSe nanocrystal superlattices | thermodynamics | ligand interaction

Self-assembly of colloidal nanocrystals (NCs) not only is a fascinating phenomenon, but also offers a promising route for design and fabrication of novel materials (1, 2). NCs possess unique size- and shape-dependent structures and properties that differ from those of their bulk counterparts (3). Analogous to formation of a crystal from constituent atoms/ions, highly uniform NCs can self-assemble into periodically ordered structures, referred to as superlattices or "artificial crystals." In addition to the unique properties of individual NCs, these NC superlattices manifest new collective behavior [such as electronic, plasmonic, magnetic, and catalytic properties (4)] through near-field coupling of neighboring NCs (5). In the past two decades, various NC superlattices were developed successfully via the controlled assembly of colloidal nanoparticles (2, 6–14), and, at the same time, extensive simulation efforts have been devoted to understanding this complicated process and to predict the assembly patterns (15–17). To achieve rational design of NC superlattices, however, it is essential to have a fundamental understanding of the mechanisms underlying their formation, including their energetics of formation and polymorphism, which form the focus of this study.

Colloidal NCs usually are composed of a hard inorganic core and a soft shell of organic molecules. The organic shell helps stabilize the inorganic core, allows the formation of an almost monodisperse size distribution of NCs, and enables dispersion of NCs in an organic solvent. NC superlattices can be synthesized, starting with well-dispersed NCs in a solvent via slow and controlled solvent evaporation. We chose PbSe as a model system because of the relative ease of preparing NC building blocks. In addition, PbSe NC superlattices are of considerable interest because they have potential applications in many fields, including photovoltaics (18, 19).

Results and Discussion

PbSe NCs were prepared following a colloidal synthesis method (20), which involves injection of an Se precursor solution into a hot Pb-complex solution, yielding, as a consequence of supersaturation, nucleation and growth of PbSe NCs. Three organic coordinating molecules, diphenylphosphine (DPP), trioctylphosphine (TOP), and oleic acid (OA), were used as the capping ligands to control the size and shape of PbSe NCs. Transmission electron microscopy (TEM) (Fig. 1*A*) indicates that the as-prepared PbSe NCs are quasi-spherical and have an average diameter of 4.7 nm, consistent with absorption spectroscopic measurements (Fig. S1). High-resolution TEM (HRTEM) images along the [100] (Fig. 1*B*) and [110] (Fig. 1*C*) projections with fast Fourier transform (FFT) patterns reveal the typical morphology of truncated octahedra (Fig. 1*E*) (21). The attenuated total reflectance (ATR) spectrum (Fig. S2) confirms the surface coating of DPP, TOP, and OA molecules around the PbSe NCs. Thermogravimetric analysis (TGA) (Fig. S3) gives a weight loss of 32.13% due to decomposition of the capping ligands. The high ratios of ligand length to nanoparticle radius make the self-assembly process of these nanoparticles sensitive to solvent–ligand interactions. To assemble PbSe NC superlattices, we dispersed the above-prepared PbSe NCs into hexane or toluene and then evaporated the solvent very slowly (1.5 mL over 4 wk). Synchrotron small-angle X-ray scattering (SAXS) measurements reveal the formation of three types of superlattices (Fig. 2*A*): the supercrystals nucleated from hexane have a body-centered cubic (*bcc*) superlattice, but those nucleated from toluene consist of both body-centered tetragonal (*bct*) and face-centered cubic (*fcc*) superlattices. The *bct* supercrystals were located in the corners, whereas the *fcc* crystals were located on the flat bottom of the vial ("2" and "1" in Fig. 1*D*), respectively. Two-dimensional SAXS images show the typical spotty features in scattering rings

Significance

Different polymorphs with very similar energetics can be made by slight changes in growth conditions. This is, to our knowledge, the first direct experimental validation of a complex energy landscape for superlattice self-assembly. Our results suggest that fundamental thermodynamic driving forces can be harnessed to tailor specific superlattice assemblies of potential technological significance.

Author contributions: Z.Q., D.W., Z.W., A.N., and H.X. designed research; Z.Q., D.W., J.Z., W.H.E., and Z.W. performed research; Z.Q., D.W., J.M.B., L.D.A.S., Z.W., A.N., and H.X. analyzed data; and Z.Q., D.W., Z.W., A.N., and H.X. wrote the paper.

The authors declare no conflict of interest.

[1]To whom correspondence may be addressed. E-mail: anavrotsky@ucdavis.edu or hxu@lanl.gov.

This article contains supporting information online at www.pnas.org/lookup/suppl/doi:10.1073/pnas.1408835111/-/DCSupplemental.

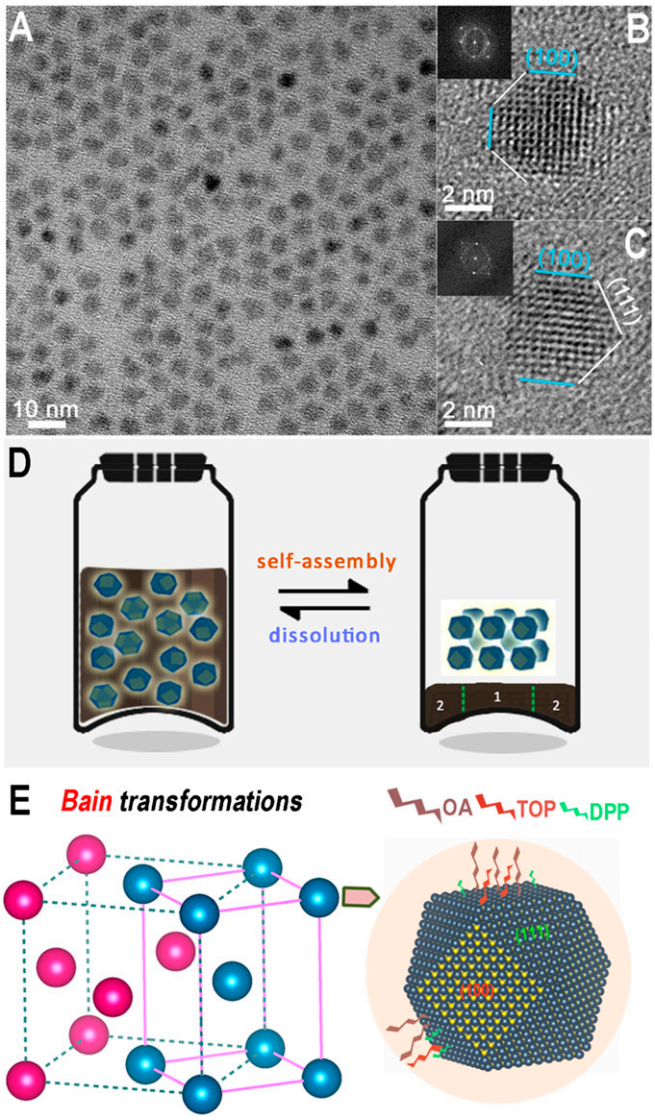

Fig. 1. (*A*) TEM image of PbSe NC building blocks. (*B* and *C*) HRTEM images of a PbSe NC and its corresponding FFT patterns along the [100] and [110] directions, respectively. (*D*) Schematic illustration of the reversible self-assembly and dissolution processes. (*E*) Schemes of Bain transformations in supercrystals and the embedded PbSe NCs.

(Fig. S4), suggesting good translational coherence and large domains of nucleated supercrystals (22, 23).

Further analyses of the SAXS data yield the following superlattice parameters (Table S1): (*i*) *bcc*: $a = b = c = 8.58$ nm; (*ii*) *bct*: $a = b = 8.32$ nm, $c = 9.81$ nm; and (*iii*) *fcc*: $a = b = 7.97$ nm, $c = 11.26$ nm. Note that for ease of description of the transformation sequence, we used a *bct* cell to describe the *bcc* and *fcc* superstructures (Fig. 1*E*). It thus becomes obvious that the *bct* superlattice represents an intermediate phase between the two end members, *bcc* and *fcc*. This sequence (*fcc-bct-bcc*) is similar to that in the so-called Bain deformation (stress-induced structural changes) observed in atomic crystals and block copolymers (24). A decrease in *a* together with an increase in *c* along the *bcc-bct-fcc* path results in the increase of c/a [$1 \rightarrow 1.179 \rightarrow \sqrt{2}(1.414)$]. Correspondingly, the nearest inter-NC spacing (d_n) increases from 7.39 to 7.66 to 7.96 nm, and the packing efficiency of hard PbSe NC cores decreases from 17.2% (*bcc*) to 16.0% (*bct*) to 15.2% (*fcc*) (see *Supporting Information* for calculation details).

To determine stability relations of the three superlattice polymorphs, we performed solution calorimetric experiments at room temperature using a Calvet twin isothermal microcalorimeter with hexane as the solvent. Because dissolution (disassembly to individual dispersed NCs) of the supercrystals in hexane essentially is the reverse process of their formation, these measurements also provide insights into the superlattice formation energetics. To confirm a well-defined final state after the sample is dissolved in the solvent, we conducted parallel synchrotron SAXS measurements on a sample in a glass vial in which the supercrystals were introduced into hexane. As shown in Fig. S5, the concentration of PbSe NCs gradually increases toward the bottom end of the vial, with NCs well-dispersed in hexane in the upper portion but showing a lamellar superstructure in the lower portion. Despite this concentration gradient, the final solution states seem to be steady after a prolonged period, thereby validating the calorimetric measurements. These "dissolved" states are, in fact, disaggregated or disassembled states, with individual NCs dispersed in the solvent, but with no breaking of individual chemical bonds within each NC.

The measured enthalpies of disassembly (ΔH_x) of PbSe NC superlattices are determined by two processes (Fig. S6): (*i*) endothermic disassembly of NCs (ΔH_1 is positive), and (*ii*) exothermic solvation of individual NCs (ΔH_2 is negative). Because the measured enthalpies are endothermic, the enthalpy of disassembly is not compensated fully by the enthalpy of solvation. Thus, disassembly occurs presumably because of an entropic driving force. As shown in Table 1, the ΔH_x values of all three superlattices are on the order of 2 kJ/mol of NCs, comparable to the energy of van der Waals interactions (23, 25, 26). The *bcc* superlattice has the highest ΔH_x and thus is energetically the most stable. The enthalpies of superlattice transformations from *fcc* and *bct* to *bcc* are -0.32 ± 0.08 and -0.55 ± 0.05 kJ/mol, respectively. These values indicate that the energetic stability decreases in the order *bcc-bct-fcc*, which is consistent with the trend of increasing inter-NC distances (Fig. 2*B*). Moreover, the small transformation enthalpies explain the formation of different superlattice polymorphs upon small perturbations to their synthesis conditions. Thus, the energies of both the self-assembly from dispersed NCs and the polymorphism define a dense energy landscape with driving forces on the order of thermal energy or smaller. As for the change in entropy (ΔS), the value should be very small in these NC supercrystals in the forms of solids and at room temperature. It is reasonable to infer that the trend in ΔH should be the same as that in Gibbs free energy (ΔG).

Our synthesis of three superlattice polymorphs of PbSe NCs and clarification of their energetic relations provide new insights into the NC interactions that control nucleation and growth of NC supercrystals. In our assembly experiments, except for using two different solvents (hexane and toluene), we kept all other conditions the same during the formation of the three polymorphs. Thus, the formation of different NC superlattices apparently is a result of the small thermodynamic differences induced by different solvents. Based on Hansen parameter calculations (27), aliphatic hexane consists of a straight, nonpolar hydrocarbon chain, whereas aromatic toluene contains one aromatic ring with a slight polarization. Of the three kinds of capping ligands (OA, DPP, and TOP), OA has the longest hydrocarbon chain, so interactions between neighboring OA chains probably play a dominant role in the NC assembly process. Although both hexane and toluene are considered "good" solvents for OA in terms of full permeation of their ligand coronas to PbSe NC surfaces (17), the nonpolar hydrocarbon chain of OA is solvated more effectively in nonpolar hexane than in the slightly polar toluene (28, 29). More specifically, as the inter-NC surface distance decreases to less than twice the OA length, the use of hexane as the solvent may result in a relatively large degree of ligand penetration. Without consideration of surface ligands, the

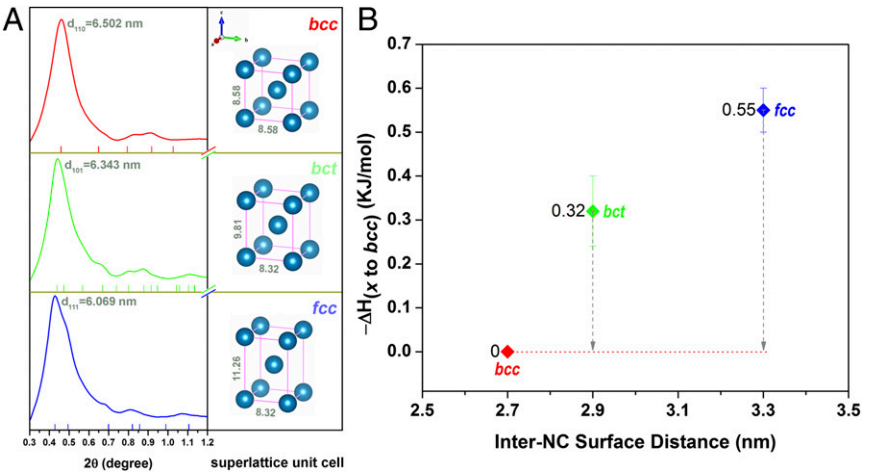

Fig. 2. (*A*) SAXS patterns of *bcc*, *bct*, and *fcc* PbSe NC supercrystals (*Left*) and their corresponding superlattice unit cells (*Right*). (*B*) The energy landscape of PbSe NC superlattice polymorphs with respect to their nearest inter-NC surface distance.

"naked" truncated octahedral PbSe NCs favor forming a *bcc* lattice that maximizes the packing density of hard cores, according to the recent theoretical investigation by Glotzer and coworkers (15). As PbSe NCs approach more closely, the morphological effect of the NC cores plays a more important role in the formation of the final NC superlattice. It thus is understandable that the *bcc* superlattice with the shortest inter-NC distance nucleated from hexane is the most stable assembly form. The homogeneous distribution of *bcc* supercrystals across the entire vial supports such an assumption. In the case of toluene, less penetration of surface-capping OAs occurs and results in larger inter-NC distances that weaken the shape-related effect, and thus enable the formation of the *fcc* superlattice ("1" in Fig. 1*D*). However, the stress distributions across the dried samples are different. At the flat bottom of the vial ("1" in Fig. 1*D*), large uniform compressive stress exists and is normal to the deposition surface. This unidirectional compressive stress distorts the ideal *fcc* lattice into the low lattice symmetry of *bct*. However, for the supercrystals at the sidewall, stress appears along both the sidewall and curved bottom, and accordingly maintains the stability of the *fcc* superlattice ("2" in Fig. 1*D*). Previous calculations indicate that *bcc* has a higher packing efficiency of 17.2% than that of *fcc* with 15.2%. The location-related variations of stress distribution cannot deform the denser *bcc* nucleated in hexane, but are large enough to transform the low-density *fcc* into the slightly higher-density phase of *bct* for the coexistence and separation of the two superlattice phases in toluene. Hence, small differences in free energy among various superlattices enable the large impact of slight stress variations on the formation of supercrystal polymorphs.

Conclusions

In summary, we assembled three distinct superlattices of PbSe NCs—*fcc*, *bct*, and *bcc*—by manipulating NC–ligand interactions via a delicate choice of solvent (hexane and toluene). Using solution calorimetry with hexane as the solvent, we measured their enthalpies of disassembly and thus determined their stability relations. The results represent the first direct measurement, to our knowledge, of the energetics of superlattice assembly/disassembly from/into their constituent NCs. The observed weak NC interactions provide the basis for making a large variety of NC superlattice polymorphs by fine-tuning their synthesis conditions.

Table 1. Enthalpies of disassembly of PbSe NC supercrystals in hexane and enthalpies of superlattice transformations from *bct* and *fcc* to *bcc* (per mole of PbSe) at 25 °C

Superlattice	ΔH_x, kJ/mol	ΔH_x, k_BT	$\Delta H_{(x \text{ to } bcc)}$, kJ/mol
bcc	2.19 ± 0.03 (4)	0.883 ± 0.012 (4)	0
bct	1.87 ± 0.07 (4)	0.754 ± 0.028 (4)	−0.32 ± 0.08
fcc	1.64 ± 0.04 (4)	0.662 ± 0.016 (4)	−0.55 ± 0.05

Values in parentheses are the number of experiments for each sample; uncertainty is two SDs of the mean.

Materials and Methods

Synthesis of PbSe NCs. PbSe NC building blocks were synthesized by a method described by Steckel et al. (20). The transparent Se precursor solution was prepared by mixing and aging 1.12 g of Se powder (200 mesh, 99.999%; Alfa Aesar), 0.13 mL of DPP (98%; Sigma–Aldrich), and 14.87 mL of TOP (90%; Fluka) at room temperature for several hours. In a typical synthesis procedure, 1.58 g of lead acetate trihydrate (99.999%; Sigma–Aldrich), 13.14 g of 1-octadecene (90%; Sigma–Aldrich), and 3.42 g of OA (90%; Aldrich) were heated to 120 °C under low pressure (10^{-3} bar) for ∼3 h. Subsequently, the as-prepared Se solution was injected into this transparent lead precursor solution (20.5 mL) at 180 °C to initiate the nucleation process of PbSe NCs, followed by continuous growth at a constant temperature of 150 °C for 20 s. Finally, the reaction mixture was quenched with 15 mL of butanol (99.8% anhydrous; Sigma–Aldrich) to obtain PbSe NCs with an average particle size of 4.7 nm. This synthesis was performed in a water- and oxygen-free environment via the use of a Schlenk line. The crude product was washed twice by precipitation with methanol (99.8% anhydrous; Sigma–Aldrich), centrifugation, and redispersion of the sediment in toluene (99.8% anhydrous; Sigma–Aldrich). The final products were well dissolved in both toluene and hexane (≥99% anhydrous; Sigma–Aldrich) for self-assembly purposes.

Self-Assembly of PbSe NCs. The set of experiments was based on a common evaporation-induced self-assembly process. Typically, 70 mg of PbSe NCs were dissolved separately in 1.5 mL of toluene and hexane solvents to produce concentrated PbSe NC suspensions and then were transferred to two vials (capacity: 2 mL). The vials were sealed with plastic caps; then, three and seven tiny holes were made in these caps for toluene and hexane solvents, respectively. The number of holes for each solvent was determined based on several trials, with the aim of producing the same evaporation rate for these two solvents. Then, the vials were kept at room temperature without any intervention, and it took around 4 wk to evaporate both solvents completely. The final PbSe NC assemblies were deposited mainly on the internal wall and bottom of the vials and were picked up for further characterization.

Solution Calorimetry. The enthalpies of disassembly of the PbSe supercrystals in hexane were determined by using a Calvet twin microcalorimeter (Setaram C80) equipped with a custom-made setup. Loosely hand-pressed pellets of PbSe supercrystals (∼4 mg) were dropped into hexane (∼4 g) maintained at 25 ± 0.5 °C. Dropping the sample pellets generated a heat effect associated with the disassembly of the PbSe supercrystals to individual nanoparticles in hexane. The normal return of the calorimetric signal to its baseline indicated the

completion of reaction in 10–15 min. The final state of this measurement is a totally disassembled PbSe supercrystal with PbSe NCs separately dispersed in hexane, similar to the starting PbSe NC colloidal solution used for self-assembly experiments. The reproducibility of these thermochemical measurements is documented as error bars in Fig. 2*B* and as errors (SDs of the mean) in Table 1.

TEM Images. TEM and HRTEM images were obtained using an FEI Tecnai F30 microscope equipped with a field emission gun and operated at 300 keV.

Ultraviolet–Visible-Near Infrared Absorption. Absorbance characterization was performed using a PerkinElmer Lambda 900 (UV/VIS/NIR) spectrometer. PbSe NCs were dispersed in tetrachloroethylene (≥99% anhydrous; Sigma–Aldrich) for this measurement.

ATR Spectra. ATR spectra were obtained on a Nicolet FTIR microscope with an mercury cadmium telluride (MCT)-A detector, on which ATR mode was used and the sample was in the solid state.

TGA. TGA experiments were performed using a Netzsch STA 449 system to measure the weight loss and chemical stoichiometry of as-prepared PbSe NCs. Approximately 10 mg of sample was hand-pressed into pellets, placed into a Pt crucible, and heated from 30 °C to 800 °C in argon at a rate of 10 °C·min^{-1}. Buoyancy correction was performed by running TGA on empty Pt crucibles under the same experimental conditions.

SAXS. Synchrotron SAXS characterizations were carried out at B_1 station of Cornell High Energy Synchrotron Source using an angle-dispersive synchrotron X-ray technique (22). Several pieces of PbSe NC supercrystals were loaded into a sample chamber (200 μm in diameter and 100 μm in thickness) seated on the flat surface of one transparent diamond window for measurements. By using a double crystal monochromator, the white X-rays were collimated into a monochromatic beam at a wavelength of 0.48596 Å. A large MAR345 detector was used to record the scattered signals from the samples. By using Fit2D software, >the 2D images were integrated into 1D patterns with intensity as a function of 2θ (deg) for structural analysis.

ACKNOWLEDGMENTS. We thank Weizhong Han and Wei Gao for assistance with the TEM and ATR measurements and Welley Siu Loc for help with the figure drawing. Z.Q. acknowledges a J. Robert Oppenheimer fellowship supported by the laboratory-directed research and development program of Los Alamos National Laboratory, which is operated by Los Alamos National Security LLC under Department of Energy (DOE) Contract DE-AC52- 06NA25396. Calorimetry at University of California, Davis was supported by the DOE Office of Basic Energy Sciences, Grant DEFG02-05ER15667. Cornell High Energy Synchrotron Source is supported by National Science Foundation Award DMR-0936384. W.H.E. and L.D.A.S. acknowledge the Dutch Foundation for Fundamental Research on Matter for supporting the program "Control over Functional Nanoparticle Solids."

1. Whitesides GM, Grzybowski B (2002) Self-assembly at all scales. *Science* 295(5564): 2418–2421.
2. Murray CB, Kagan CR, Bawendi MG (1995) Self-organization of CdSe nanocrystallites into three-dimensional quantum dot superlattices. *Science* 270(5240):1335–1338.
3. Alivisatos AP (1996) Semiconductor clusters, nanocrystals, and quantum dots. *Science* 271(5251):933–937.
4. Talapin DV, Lee J-S, Kovalenko MV, Shevchenko EV (2010) Prospects of colloidal nanocrystals for electronic and optoelectronic applications. *Chem Rev* 110(1):389–458.
5. Wang T, et al. (2012) Self-assembled colloidal superparticles from nanorods. *Science* 338(6105):358–363.
6. Macfarlane RJ, Jones MR, Lee B, Auyeung E, Mirkin CA (2013) Topotactic interconversion of nanoparticle superlattices. *Science* 341(6151):1222–1225.
7. Rycenga M, McLellan JM, Xia Y (2008) Controlling the assembly of silver nanocubes through selective functionalization of their faces. *Adv Mater* 20(12):2416–2420.
8. Quan Z, Fang J (2010) Superlattices with non-spherical building blocks. *Nano Today* 5(5):390–411.
9. Black CT, Murray CB, Sandstrom RL, Sun S (2000) Spin-dependent tunneling in self-assembled cobalt-nanocrystal superlattices. *Science* 290(5494):1131–1134.
10. Sun S, Murray CB, Weller D, Folks L, Moser A (2000) Monodisperse FePt nanoparticles and ferromagnetic FePt nanocrystal superlattices. *Science* 287(5460):1989–1992.
11. Yin Y, Xia Y (2003) Self-assembly of spherical colloids into helical chains with well-controlled handedness. *J Am Chem Soc* 125(8):2048–2049.
12. Tao A, Sinsermsuksakul P, Yang P (2007) Tunable plasmonic lattices of silver nanocrystals. *Nat Nanotechnol* 2(7):435–440.
13. Xia Y, et al. (2011) Self-assembly of self-limiting monodisperse supraparticles from polydisperse nanoparticles. *Nat Nanotechnol* 6(9):580–587.
14. Tang Z, Zhang Z, Wang Y, Glotzer SC, Kotov NA (2006) Self-assembly of CdTe nanocrystals into free-floating sheets. *Science* 314(5797):274–278.
15. Damasceno PF, Engel M, Glotzer SC (2012) Predictive self-assembly of polyhedra into complex structures. *Science* 337(6093):453–457.
16. Knorowski C, Burleigh S, Travesset A (2011) Dynamics and statics of DNA-programmable nanoparticle self-assembly and crystallization. *Phys Rev Lett* 106(21): 215501.
17. Kaushik AP, Clancy P (2013) Solvent-driven symmetry of self-assembled nanocrystal superlattices—a computational study. *J Comput Chem* 34(7):523–532.
18. Wise FW (2000) Lead salt quantum dots: The limit of strong quantum confinement. *Acc Chem Res* 33(11):773–780.
19. Semonin OE, et al. (2011) Peak external photocurrent quantum efficiency exceeding 100% via MEG in a quantum dot solar cell. *Science* 334(6062):1530–1533.
20. Steckel JS, Yen BKH, Oertel DC, Bawendi MJ (2006) On the mechanism of lead chalcogenide nanocrystal formation. *J Am Chem Soc* 128(40):13032–13033.
21. Simon P, et al. (2012) PbS-organic mesocrystals: The relationship between nanocrystal orientation and superlattice array. *Angew Chem Int Ed* 51(43):10776–10781.
22. Wang Z, et al. (2010) Integrating in situ high pressure small and wide angle synchrotron x-ray scattering for exploiting new physics of nanoparticle supercrystals. *Rev Sci Instrum* 81(9):093902.
23. Wang Z, et al. (2013) Correlating superlattice polymorphs to internanoparticle distance, packing density, and surface lattice in assemblies of PbS nanoparticles. *Nano Lett* 13(3):1303–1311.
24. Bain E (1924) The nature of martensite. *Trans Am Inst Min Metall Eng* 70:25–35.
25. Goodfellow BW, Patel RN, Panthani MG, Smilgies D-M, Korgel BA (2011) Melting and sintering of a body-centered cubic superlattice of PbSe nanocrystals followed by small angle X-ray scattering. *J Phys Chem C Nanomater Interfaces* 115(14):6397–6404.
26. Goodfellow BW, Korgel BA (2011) Reversible solvent vapor-mediated phase changes in nanocrystal superlattices. *ACS Nano* 5(4):2419–2424.
27. Hansen CM (2007) *Hansen Solubility Parameters: A User's Handbook* (CRC, Boca Raton, FL).
28. Flory PJ (1941) Thermodynamics of high polymer solutions. *J Chem Phys* 9(8):660.
29. Huggins ML (1941) Solutions of long chain compounds. *J Chem Phys* 9(5):440.